Compressible air entrapment in high-speed drop impacts on solid surfaces

Yuan Liu, Peng Tan and Lei Xu†

Department of Physics, The Chinese University of Hong Kong, Shatin, N.T., Hong Kong, China

Using high-speed photography coupled with optical interference, we experimentally study the air entrapment during a liquid drop impacting a solid substrate. We observe the formation of a compressed air film before the liquid touches the substrate, with internal pressure considerably higher than the atmospheric value. The degree of compression highly depends on the impact velocity, as explained by balancing the liquid deceleration with the large pressure of the compressed air. After contact, the air film expands vertically at the edge, reducing its pressure within a few tens of microseconds and producing a thick rim on the perimeter. This thick-rimmed air film subsequently contracts into an air bubble, governed by the complex interaction between surface tension, inertia and viscous drag. Such a process is universally observed for impacts above a few centimetres high.

1. Introduction

The impacts of liquid drops onto solid substrates are ubiquitous and appear in a variety of applications, such as spray coating and ice accumulation on aircraft (Yarin 2006). While the interaction between liquid and solid has been extensively studied, the important role of air was discovered only recently, as shown by the surprising finding that air pressure strongly influences the liquid splash outcomes (Xu, Zhang & Nagel 2005; Xu 2007). Therefore, understanding the behaviour of air during liquid–solid impacts will bring new advances to this fundamental phenomenon, and may benefit practical processes such as splash control and surface coating. Experimentally, entrapment of air during impacts is commonly observed: when the impact speed is high ($\sim$1 m s^{-1}), a thin air film is trapped at the very beginning, which subsequently contracts into one or two air bubbles (Thoroddsen, Etoh & Takehara 2003; Thoroddsen *et al.* 2005). At low impact speed ($\sim$0.1 m s^{-1}), however, the air under the drop remains connected with outside for the majority of time (i.e. not entirely trapped), until it gets enclosed by the moving contact line (de Ruiter *et al.* 2012). Recent study (Kolinski *et al.* 2012) further reveals a short-lived nanometre thick

air film right before the formation of the contact line. The air entrapment depends on the impact velocity, the liquid property (Thoroddsen *et al.* 2003, 2005; Kolinski *et al.* 2012; de Ruiter *et al.* 2012) and the surrounding air pressure (Driscoll & Nagel 2011). Theoretically, simulations have explored air entrapment with both compressible (Mandre, Mani & Brenner 2009; Mani, Mandre & Brenner 2010) and incompressible (Smith, Li & Wu 2003; Hicks & Purvis 2010) models. Marked deformation of the drop surface *before* it touches the solid is predicted: the drop surface is deformed upwards at the impact centre, making the first contact away from the centre on a ring-like area. The compressible model by Mandre *et al.* (2009) and Mani *et al.* (2010) further indicates significant compression in the trapped air, resulting in a pressure considerably higher than the atmospheric value. Despite these important predictions, however, experimental measurements on the exact conditions of the trapped air are still missing, especially near the critical moment of impact. In particular, even the fundamental question whether the trapped air is compressed or not remains unclear. To clarify these puzzles and better understand the impact phenomenon, an experimental study on air entrapment close to the moment of impact is highly desirable.

2. Experimental methods

Using fast photography coupled with optical interference (Driscoll & Nagel 2011; de Ruiter *et al.* 2012), we experimentally study the air entrapment during a liquid drop impacting a smooth substrate at relatively high speeds (0.7–3 m s^{-1}). We observe the formation of a compressed air film *before* the liquid touches the substrate, with internal pressure considerably higher than the atmospheric value. The degree of compression highly depends on the impact velocity, which is explained by balancing the liquid deceleration with the large pressure of the compressed air. After contact, the air film expands vertically at the edge, reducing its pressure within a few tens of microseconds and producing a thick rim on the perimeter. This thick-rimmed air film subsequently contracts into an air bubble, governed by the complex interaction between surface tension, inertia and viscous effects (see figure 5*a* for the entire process). Such a process is universally observed for impacts above a few centimetres high.

To independently study the effects of viscosity and surface tension, three different liquids are used: H$_2$O, oil-1.04 and oil-9.30. The two oils are silicone oils with similar surface tensions σ but different dynamic viscosities: $\mu = 1.04$ mPa s and 9.30 mPa s. By contrast, H$_2$O and oil-1.04 have similar viscosities but different surface tensions (see table 1). Reproducible drops around a millimetre in size (see table 1 for details) are released from rest at different heights, and impact a smooth and dry cover glass at various velocities (0.7–3 m s^{-1}). The two silicone oils completely wet the glass substrate, with zero static contact angle, and H$_2$O has a static contact angle $\theta = 65 \pm 5°$. All experiments are performed at atmospheric pressure, $P_0 = 101$ kPa. The impacts are viewed from below with an inverted microscope and recorded with a high-speed camera (Photron SA4) at recording speeds up to 150 000 frames per second. The illumination light is monochromatic, with wavelength $\lambda = 546$ nm and coherence length of a few micrometres. The short coherence length makes sure that there is no interference between the two sides of the substrate. The Newton's rings produced by the trapped air can quantitatively characterize the thickness profile of the air.

Liquid	ρ (kg m^{-3})	σ (mN m^{-1})	μ (mPa s)	θ (deg.)	R (mm)
H$_2$O	1000	50 ± 5	1.00 ± 0.01	65 ± 5	2.0 ± 0.1 (1.5 ± 0.1)
Oil-1.04	816	17.4	1.04 ± 0.01	0	1.5 ± 0.1 (1.2 ± 0.1)
Oil-9.30	930	20.1	9.30 ± 0.02	0	1.5 ± 0.1

TABLE 1. Material properties and drop radius of the various liquids. Size R is measured right before contact by fitting the local radius of curvature at the bottom of the drop. For the lowest release height, strong oscillation in the drop makes R different from the average radius in H$_2$O and oil-1.04, as shown in parentheses.

3. Experimental results

3.1. *Formation of air film before contact (t $\leqslant$ 0)*

We first clarify the entrapment behaviour *before* liquid touches solid. As the drop approaches the substrate, the air in the thin gap cannot escape immediately and gets compressed to a high pressure (exact values measured later in figure 4*b*). Such a high pressure locally pushes in the drop surface and creates a dimple around the impact centre, as illustrated by the cartoon in figure 1(*b*) inset. The interference patterns from the dimple are shown in figure 1(*a*), for an oil-9.30 drop at impact speed $V_0 = 0.74 \pm 0.01$ m s^{-1}. In the first frame (-20 µs), Newton's rings appear as the drop-to-substrate distance becomes smaller than the coherence length of light (a few micrometres). In the second frame (-13 µs), a quite flat dimple with a horizontal scale of several hundred micrometres but a vertical scale of a few micrometres is produced. Because of this thin and flat nature, the dimple can be exactly considered as an air film. The third frame (-7 µs) shows a very similar pattern as the second one, except with a few black spots of isolated contacts indicated by the white arrows. The fourth frame (0 µs) reveals the global liquid–solid contact on a thick black ring at the edge of the pattern. This moment of first global contact is also defined as the moment of $t = 0$ throughout our study.

The thickness of the dimple, H, can be accurately derived from the pattern with the relationship $\Delta H = \lambda/4 = 136.5$ nm between two neighbouring rings. Using contact area as the zero-thickness reference point, we can quantitatively determine the entire thickness profile of the trapped air in the $t = 0$ frame. We can further determine the profiles for the two previous frames ($t = -7$ µs and -13 µs), owing to their highly similar patterns as the $t = 0$ frame, which enables the tracking of every ring. The thickness as a function of distance from the centre, H versus r, is plotted in figure 1(*b*): 13 µs before the contact, an air film with the lateral size $2L_0 \cong 500$ µm but a thickness of only $H_0 \cong 3.5$ µm forms, which maintains an almost identical profile through the next several frames. Significant variation only appears near the centre ($r \cong 0$), where the interface moves *upwards* instead of downwards, with a small speed 0.02 ± 0.01 m s^{-1} (calculated from the profiles at $t = -7$ µs and $t = 0$ µs). Clearly, the motion of the drop is quite complex immediately before the contact: while the main body falls at the impact speed, $V_0 = 0.74$ m s^{-1}, the small volume above the trapped air ($2L_0 \cong 500$ µm) stays almost stationary, with the region at $r \cong 0$ even moving oppositely in the upward direction.

3.2. *Profile of air film upon contact (t = 0)*

To systematically study the air film properties, we characterize their profiles at $t = 0$ for different velocities and liquids, as shown in figure 2(*a*). The three panels
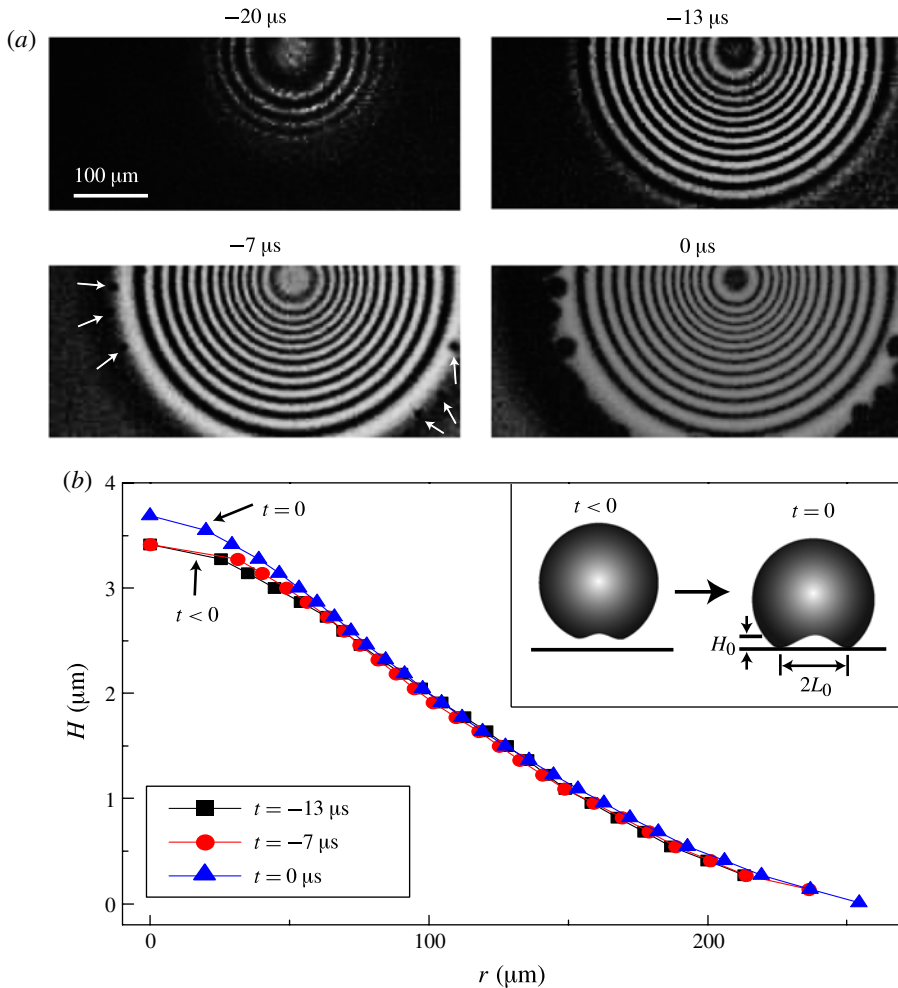
FIGURE 1. The formation of a trapped air film before liquid touches solid. (*a*) The interference patterns before contact by an oil-9.30 drop at impact velocity $V_0 = 0.74 \pm 0.01 \text{ m s}^{-1}$. The time uncertainty is half of the frame interval, 4 µs. In the first frame (-20 µs), Newton's rings appear as the drop-to-substrate distance becomes smaller than the coherence length of light. In the second frame (-13 µs), a dimple with horizontal scale of several hundred micrometres but vertical scale of a few micrometres is produced. The third frame (-7 µs) reveals a few black spots of isolated contacts at the edge (specified by the white arrows). The fourth frame (0 µs) shows the global liquid–solid contact on a thick black ring at the edge of the pattern. This moment of first global contact is also defined as the moment of $t = 0$ throughout our study. (*b*) The thickness profile, $H(r)$, constructed from the patterns in panel (*a*). Note the very different scales for the x and y axes. The curves almost overlap with each other, indicating very little motion of the interface through different frames. Significant difference only appears at impact centre ($r = 0$), where the interface moves *upwards* instead of downwards, with speed $0.02 \pm 0.01 \text{ m s}^{-1}$. The schematic in the inset illustrates a dimple with horizontal scale $2L_0$ and thickness H_0 (drawing not to scale).
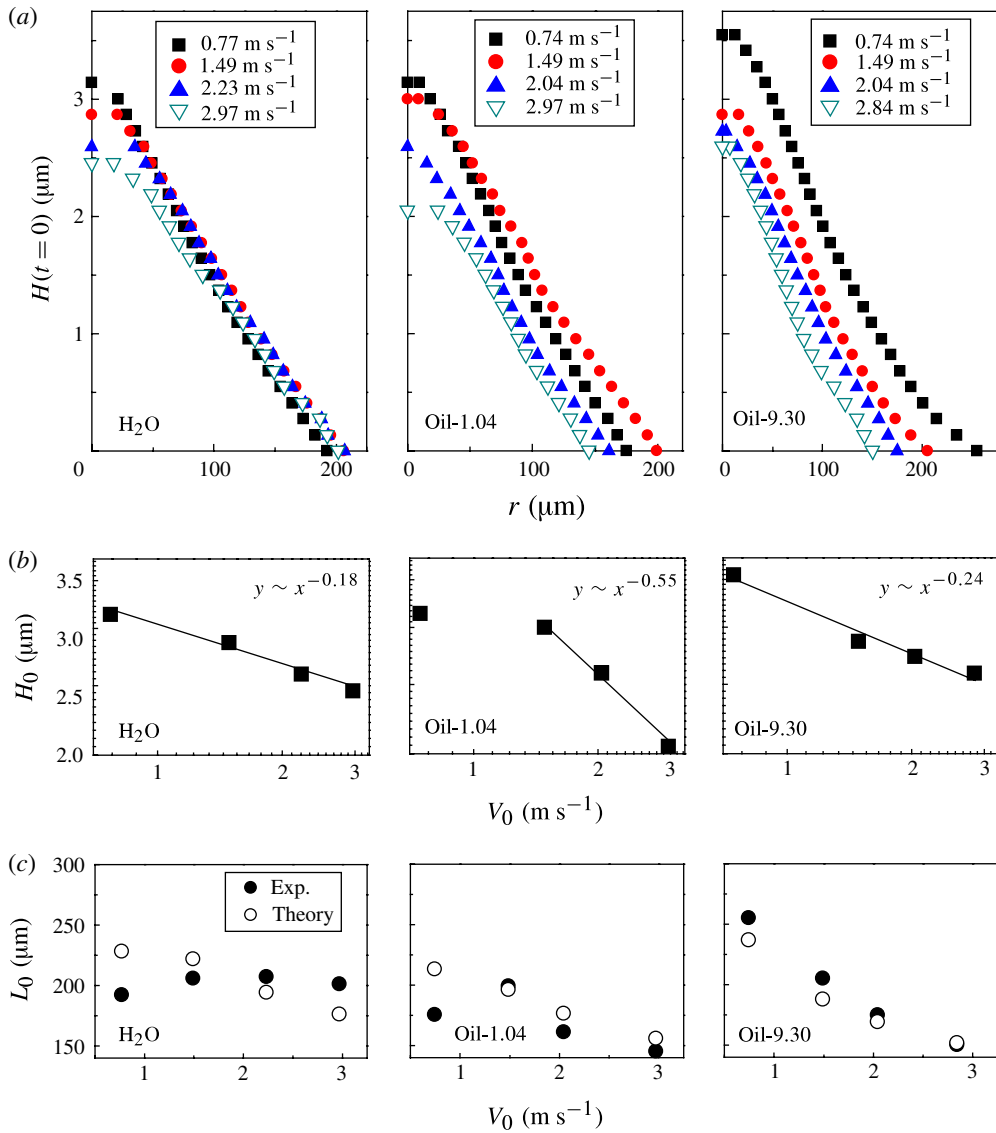
FIGURE 2. Characterizing the air film profile at $t = 0$ for different liquids and impact velocities. (*a*) Air film profiles measured at the moment of contact ($t = 0$) with Newton's rings method. The three panels show the results for H_2O, oil-1.04 and oil-9.30, respectively. Different coloured curves are measured at different V_0. (*b*) The maximum film thickness at the centre, H_0, versus the impact velocity, V_0. The solid lines are the best power-law fits within the limited data range. (*c*) The horizontal radius, L_0, versus impact velocity, V_0, in different liquids. The solid symbols are experimental measurements, while the open symbols are theoretical predictions from an incompressible model, $L_0 = 3.8 \, (4\mu_g/\rho V_0)^{1/3} R^{2/3}$ (Hicks *et al.* 2012). Good agreement is observed at high V_0.

correspond to the three different liquids, and each panel contains data for several impact velocities. In general, the air film becomes thinner with the increase of impact velocity, as illustrated by the measurements. For quantitative understanding, we plot the maximum thickness measured at $r = 0$, H_0, as a function of V_0 in figure 2(*b*). Clearly, H_0 decreases with V_0, consistent with the previous theory (Mandre *et al.* 2009). However, the exact dependence of H_0 on V_0 differs from the prediction: we calculate the 'compressibility factor' defined theoretically as $\epsilon = P_0/(R\mu_g^{-1}V_0^7\rho^4)^{1/3}$ (Mandre *et al.* 2009; μ_g is the dynamic viscosity of air), and obtain the range $\epsilon^{-1} \sim 0.1$–10 for our experimental data. Thus our experiments are at the transition region from 'incompressible regime' to 'compressible regime' predicted by the theory, and H_0 should decrease with V_0 faster than the power law of $H_0 \sim V_0^{-2/3}$. However, the log–log plots in figure 2(*b*) display powers much slower than $-2/3$. This discrepancy calls for further theoretical studies on the problem.

We also measure the horizontal radius, L_0, versus V_0 for different liquids and compare it with the existing theory (Hicks *et al.* 2012). In figure 2(*c*), we plot our measurements as solid symbols and the theoretical prediction, $L_0 = 3.8\,(4\mu_g/\rho V_0)^{1/3}R^{2/3}$ (Hicks *et al.* 2012), as the open symbols. We use the bottom radius of curvature immediately before contact shown in table 1 for the calculation. Without any fitting parameter, a reasonable agreement is observed at high V_0, while some deviation occurs for low V_0. This is surprising since the theory is based on an incompressible calculation, which should match our low-V_0 rather than the high-V_0 region. Further study is required to clarify this puzzle.

3.3. *Evolution of air film after contact ($t \geqslant 0$)*

The dimple continues to evolve *after* the liquid–solid contact. The interference patterns for $t \geqslant 0$ are shown in figure 3(*a*), for an impact with the same conditions as in figure 1(*a*). Frame one (0 μs) shows the Newton's rings from the initial thin film, with the global contact on a thick black ring at the edge. During the subsequent contraction (28–139 μs), the Newton's rings in the middle remain largely unchanged, while a grey region without rings grows thicker and thicker at the edge. This grey region smoothly evolves into an air bubble at the end of the process (319 μs and 2486 μs). Such a smooth evolution implies that the thickness of the grey region at $t = 319$ μs must be close to the bubble diameter ($d = 76$ μm) and substantially exceed the coherence length of light, which explains the lack of Newton's rings. Similarly, having a thickness larger than the coherence length explains the absence of rings in the grey region for the previous frames as well. To estimate the thickness there, we assume that the grey region has a semicircular vertical cross-section, as demonstrated by the dashed curves in figure 3(*b*) (the non-circular impression comes from the different x and y scales).

Combining the thickness measured from the Newton's rings and estimated at the grey region, we plot the entire thickness profiles for the $t \geqslant 0$ frames in figure 3(*b*). Different colours indicate different times t, with the solid symbols from direct measurement and the dashed curves from the semicircular estimate. Clearly the air film does not contract with a uniform thickness; instead, the edge grows into a thick rim while the interior remains thin and flat.

3.4. *The compression at $t = 0$*

Is the trapped air initially ($t = 0$) compressed or not? We address this fundamental question by accurately measuring and comparing the volumes at the initial ($t = 0$) and the final states. The volume at $t = 0$ is directly obtained from the thickness
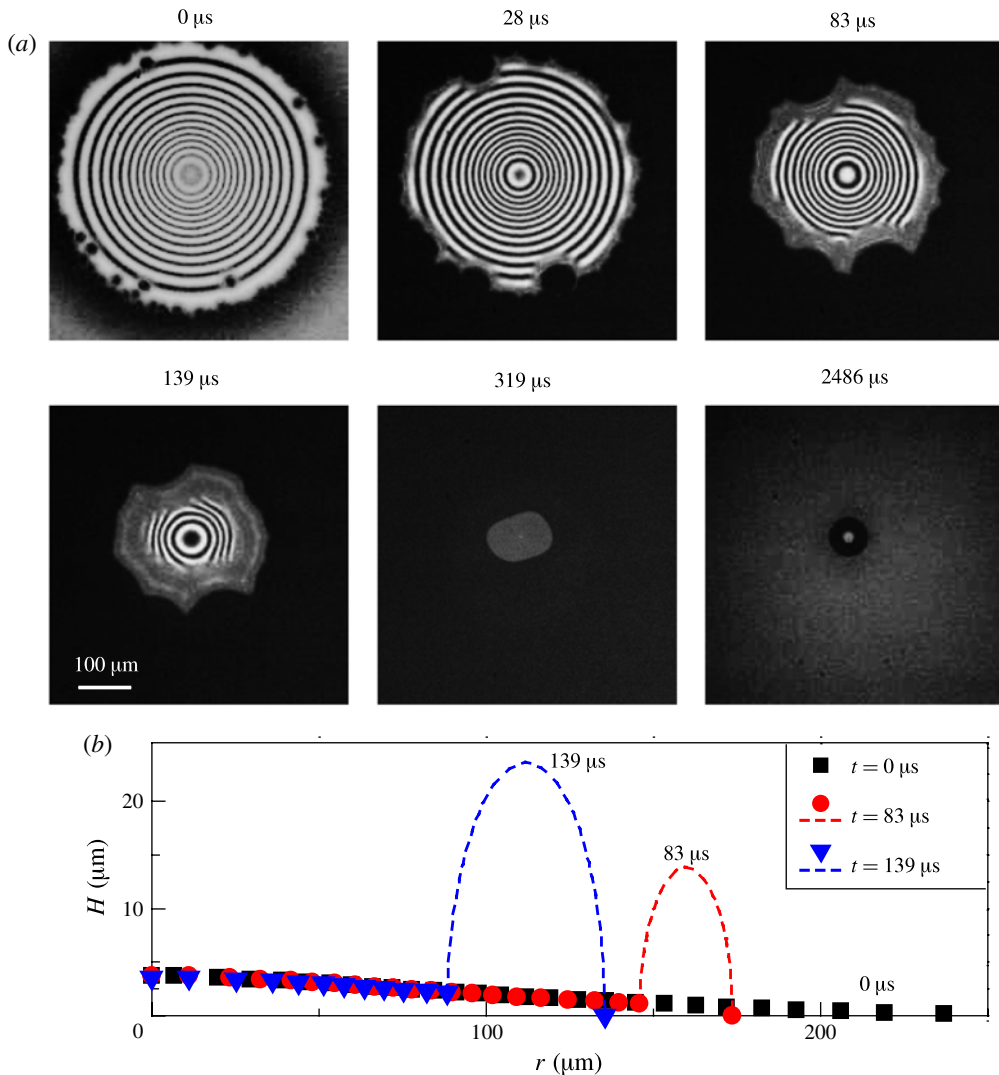
FIGURE 3. The evolution of trapped air after impact. The time uncertainty is half of the frame interval, 7 µs. (*a*) The interference patterns for $t \geqslant 0$ by an oil-9.30 drop at $V_0 = 0.74 \pm 0.01$ m s^{-1}. Frame one (0 µs) shows the Newton's rings from the trapped thin air film, with the thick black ring at the edge indicating global liquid–solid contact. During the subsequent contraction (28–139 µs), the Newton's rings in the middle remain largely unchanged, while a grey region without rings grows thicker and thicker at the edge. This grey region smoothly evolves into an air bubble with diameter $d = 76 \pm 3$ µm (319 and 2486 µs). (*b*) The thickness profiles from the centre towards the edge along one typical radial direction. From the patterns in panel (*a*), we derive the solid symbols using the Newton's rings, and estimate the grey region's profile with semicircles as plotted by the dashed curves (although the different scales in *x* and *y* axes produce a non-circular impression). We emphasize that the dashed curves are from an estimate and thus cannot be taken as serious measurements.
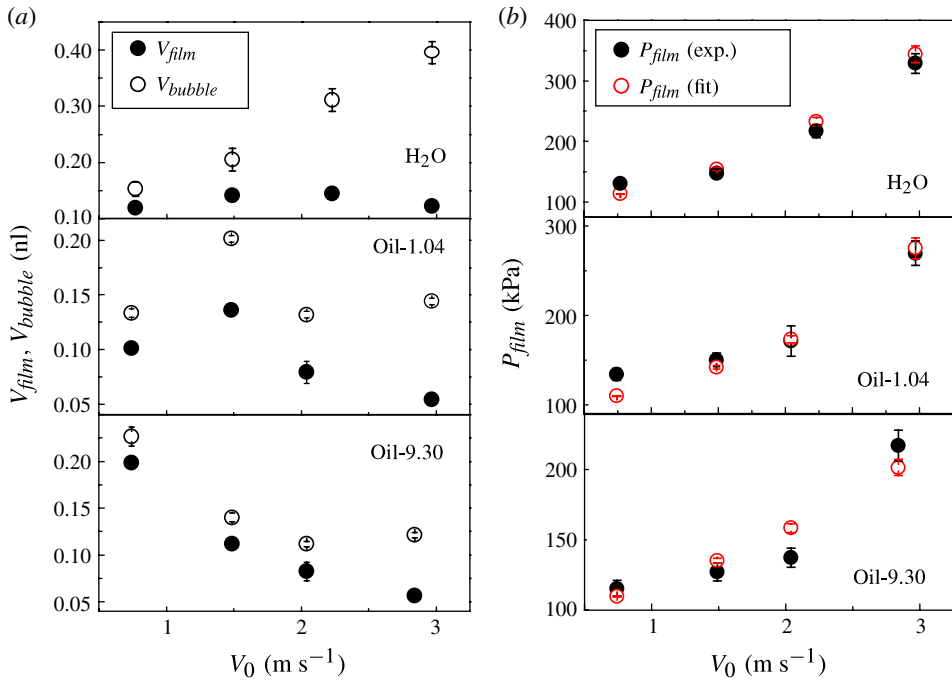
FIGURE 4. Characterizing the initial pressure (i.e. at $t = 0$) for different liquids and impact velocities. (*a*) The volume of the initial air film, V_{film}, and the final air bubble, V_{bubble}, versus the impact velocity V_0 in different liquids. Clearly the difference between V_{film} and V_{bubble} increases with V_0. (*b*) The pressure of the air film at $t = 0$. The solid symbols come from volume measurements (equation (3.1)) and the open symbols are calculated from equation (3.2). They agree reasonably well. The fitting parameter, C, has the values $C = 0.33$ (H_2O), 0.33 (oil-1.04) and 0.23 (oil-9.30). It does not change with surface tension but decreases with viscosity.

profile $H(r)$; and the volume of the final air bubble is accurately determined from its diameter. To make sure that the bubble is a perfect sphere instead of a cap intersected by the substrate, we keep track of the bubble until it leaves the surface and rises upwards. Since the bubble is a perfect sphere after leaving the surface, we can unambiguously determine its volume from the diameter. The exact values of V_{film} and V_{bubble} are shown in figure 4(*a*) for different velocities and liquids. The plot reveals a considerable volume increase from film to bubble, proving that the trapped air at $t = 0$ is indeed *compressed*.

To further estimate the pressure at $t = 0$, we need to clarify whether the compression is isothermal or adiabatic. This depends on the time scale of air entrapment, τ, compared with the time scale during which thermal equilibrium can be reached, τ'. In our experiment, $\tau \sim H_0/V_0 \sim 1\,\mu s$; while τ' is determined by the rate of thermal conduction. Our system is a thin air film with the upper and lower boundaries (liquid drop and glass substrate respectively) at room temperature. Suppose there is a temperature change ΔT in the middle (from gas compression or viscous heating or other reasons). The thermal gradient then becomes $\Delta T/(H_0/2)$ and the heat flux per unit time is $dQ/dt \sim 2kA\Delta T/(H_0/2)$, with k being the thermal conductivity of air and A being the horizontal cross-sectional area; the factor of 2

comes from the existence of two boundaries. This heat flux will bring the system back to equilibrium during the time scale: $\tau' \sim c_p \rho_{air} v_{air} \Delta T/(\mathrm{d}Q/\mathrm{d}t) \sim c_p \rho_{air} H_0^2/12k$, with c_p being the air's specific heat per unit mass and $v_{air} \sim (AH_0)/3$ being the volume of trapped air. Plugging in the values for atmospheric pressure and room temperature, $c_p = 10^3$ J (kg K)$^{-1}$, $\rho_{air} = 1.2$ kg m^{-3}, $k = 0.026$ J (s m K)$^{-1}$, we obtain $\tau' \sim 0.03$ μs $\ll \tau \sim 1$ μs. Therefore, the trapped air reaches thermal equilibrium rather rapidly, because of its thinness and small heat capacity, and the compression in our experiment can be considered as *isothermal*. Subsequently, the compressed air film expands to an uncompressed air bubble, again in an isothermal manner since expansion is even slower than compression. Thus we can obtain the initial air film pressure, P_{film}, from the isothermal equation of state:

$$P_{film} = P_{bubble} \frac{V_{bubble}}{V_{film}} = P_0 \frac{V_{bubble}}{V_{film}}. \tag{3.1}$$

Here $P_{bubble} = P_0 = 101$ kPa since the bubble is uncompressed (the curved surface of the bubble adds a negligibly small Laplace pressure around 1 kPa to P_{bubble}). The exact values of P_{film} are shown as solid symbols in figure 4(*b*). Apparently, P_{film} increases dramatically with impact speed, varying from very close to P_0 to several P_0.

This velocity dependence can be qualitatively understood by a force balance estimate. Immediately before the contact, the compressed air in the dimple locally decelerates the liquid to an almost complete stop in the vertical direction (see figure 1*b* main panel), on the length scale of the dimple's radius L_0 (see figure 1*b* inset). The deceleration occurs during the time scale $\tau \sim H_0/V_0$, with the magnitude $a \sim V_0/\tau \sim V_0^2/H_0$. Since the affected liquid has mass $m \sim \rho L_0^3$, we get the force $f = ma \sim C\rho L_0^3 V_0^2/H_0$, with C being a pre-factor of order unity. This force naturally comes from the excess pressure of compressed air multiplying the area, $f \sim (P_{film} - P_0)L_0^2$. Making the two force expressions equal (Mandre *et al.* 2009; Mani *et al.* 2010) and solving for P_{film} yields

$$P_{film} = P_0 + C\rho V_0^2 \frac{L_0}{H_0}. \tag{3.2}$$

This expression has the same trend as the measurements: at small V_0, P_{film} approaches P_0; while it rises rapidly with V_0 due to the large geometric factor, $L_0/H_0 \sim 100 \gg 1$. The values calculated from this expression are plotted as open symbols in figure 4(*b*), and agree reasonably well with the measurements (solid symbols), for different liquids at various impact speeds. The only fitting parameter, C, is indeed of order unity: $C = 0.33$ (H$_2$O), 0.33 (oil-1.04) and 0.23 (oil-9.30). Clearly C does not change with surface tension but decreases with viscosity, suggesting that under the same impact conditions the air trapped in a more viscous drop is less compressed.

Comparing with the existing compressible model (Mandre *et al.* 2009; Mani *et al.* 2010), our experimental range overlaps with their transition region from 'incompressible regime' to 'compressible regime' (i.e. $0.1 < \epsilon^{-1} < 10$). Indeed, the data in figure 4(*b*) verify such a predicted transition: at low V_0 the pressure is close to P_0 and the compression is small; while significant compression appears above $V_0 \sim 1.5$ m s^{-1} (corresponding to $\epsilon \sim 1$ in the theory). We also find that the initial impact pressure, P_{film}, exceeds the liquid inertia, ρV_0^2, by a large factor of $L_0/H_0 \sim 100$. This comes from the dramatic deceleration of the liquid under the thin gap geometry.
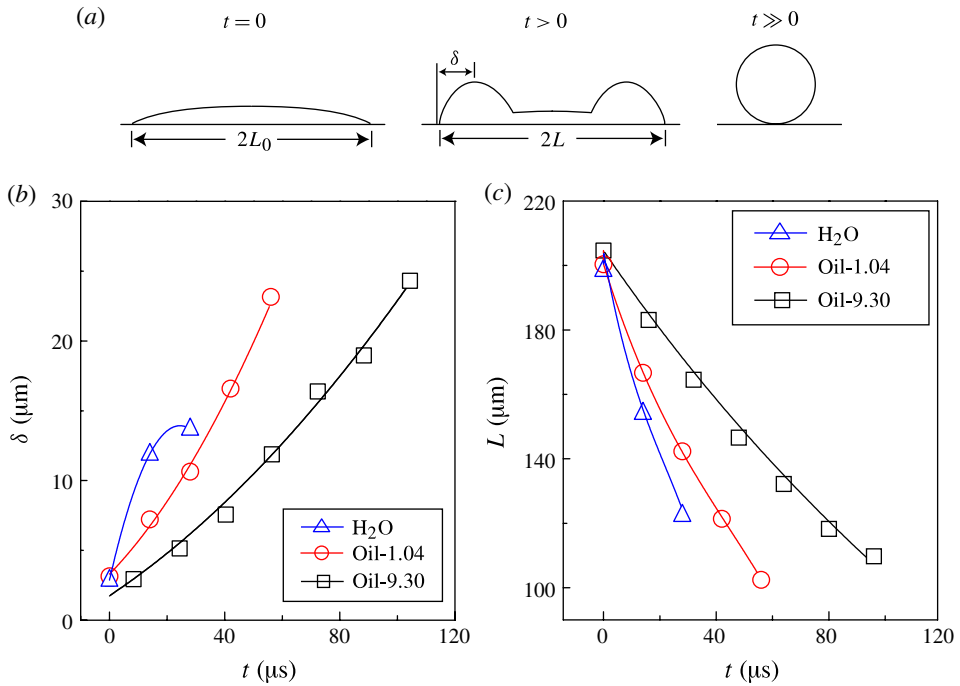
FIGURE 5. Evolution of trapped air during contraction. (*a*) Schematic illustrating the vertical profile evolution during contraction. The air film turns into an uncompressed thick-rimmed structure within a few tens of microseconds, and then contracts into an air bubble. (*b*) Measuring $\delta(t)$ experimentally. The three curves come from the three liquids at the same impact velocity, $V_0 = 1.49 \pm 0.02$ m s^{-1}. The open symbols are our measurements and the solid curves are high-order polynomial fits. These functions are plugged into (3.4) to calculate $L(t)$. (*c*) The comparison of $L(t)$ between the measurements and the calculation. The open symbols come from direct measurements while the curves are calculated from (3.4). With the same fitting parameters, $C_1 = 0.63$ and $C_2 = 1.54$, we obtain excellent agreement for different liquids. The air film contracts the fastest in H_2O, owing to the large surface tension and low viscosity. It contracts more slowly in oil-1.04, because of the reduced surface tension. The motion is the slowest in oil-9.30, owing to the effects of both low surface tension and high viscosity.

3.5. *The contraction at* $t > 0$

From compressed air film to uncompressed air bubble, the detailed process requires further clarification. We measure this process from interference patterns and demonstrate the evolution in figure 5(*a*). At the moment of contact ($t = 0$), the trapped air is thin and flat with a pressure higher than P_0. After the contact ($t > 0$), however, the air pressure drops sharply as the impact pressure decreases, resulting in a rapid volume expansion at the edge of the film. This non-uniform expansion may come from the non-uniform pressure distribution after contact: the centre of the film is right below the stagnation point of the liquid and thus experiences higher impact pressure; while the edge of the air film experiences less impact pressure and is more easy to expand. This expansion produces a rim much thicker than the interior, as illustrated in figure 5(*a*). We estimate the rim's volume by assuming a semicircular profile and deduce the pressure from the volume estimate. We find that the pressure rapidly drops

to the uncompressed value within a few tens of microseconds. The uncompressed thick-rimmed structure subsequently contracts into an air bubble.

Therefore, the contraction process is mostly under the uncompressed condition, except at the very beginning, consistent with the incompressible assumption in previous contraction measurements (Thoroddsen *et al.* 2003, 2005). However, the previous study assumes a uniform film thickness, while we believe that the thick rim plays an important role. We take the characteristic size of the rim, δ (see figure 5a), as the dominant length scale during contraction: the surface tension provides the driving stress, σ/δ, which is balanced by the liquid inertial stress, ρv^2, and the viscous stress, $\mu v/\delta$. We note that the buoyant effect may also drive the dewetting of the air film. However, when compared with the surface tension, the buoyant effect is completely negligible during the contraction period studied here: $\Delta\rho V g/A \sim 0.1$ Pa $\ll \sigma/\delta \sim 10^3$ Pa. Therefore, we neglect the buoyant effect and use the surface tension as the sole driving force:

$$\frac{\sigma}{\delta(t)} = C_1 \rho v\,(t)^2 + C_2 \mu \frac{v(t)}{\delta(t)}. \tag{3.3}$$

Here $v(t)$ is the instantaneous contraction velocity at the edge, and C_1 and C_2 are pre-factors of order one. This expression relates the contraction speed $v(t)$ to the rim size $\delta(t)$. From $v(t)$, we can further calculate the pattern's radius, $L(t)$ (see figure 5a), via the relationship $v(t) = -\mathrm{d}L(t)/\mathrm{d}t$. Thus we can obtain $L(t)$ by solving for $v(t)$ in (3.3) and then integrating it:

$$L(t) = L_0 - \int_0^t v(\tau)\,\mathrm{d}\tau$$

$$= L_0 - \int_0^t \frac{-C_2\mu + \sqrt{C_2^2\mu^2 + 4C_1\rho\sigma\delta(\tau)}}{2C_1\rho\delta(\tau)}\,\mathrm{d}\tau. \tag{3.4}$$

Therefore, $L(t)$ can be calculated from the knowledge of $\delta(\tau)$. We obtain the function $\delta(\tau)$ by first measuring δ experimentally and then fitting the data with high-order polynomials, as shown in figure 5(b). On the other hand, $L(t)$ can be independently measured from our images. To measure $L(t)$ directly, we make the best circular fit for the edge of the pattern, and obtain $L(t)$ from the radius of the circle. The results of the two approaches are compared in figure 5(c) for different liquids. The calculated curves match the measured symbols quite well, confirming the validity of the expression in (3.3). In addition, the two fitting parameters, $C_1 = 0.63$ and $C_2 = 1.54$, are universally valid for all liquids, and are indeed of order unity. The air film contracts the fastest in H_2O, owing to the large surface tension and low viscosity. It contracts more slowly in oil-1.04, because of the reduced surface tension. The motion is the slowest in oil-9.30, owing to the effects of both low surface tension and high viscosity. In conclusion, the contraction is determined by the complex interaction between surface tension, inertia and viscous effects, as described by (3.3). Because the dynamic contact angle during contraction is different from the static value and cannot be measured directly, its role for air film contraction is still unclear.

4. Conclusions

In this work, we couple high-speed photography with optical interference to study the formation and evolution of air entrapment in liquid–solid impacts. We find that a compressed air film forms before liquid touches solid, with an internal pressure

significantly higher than the atmospheric value. After contact, the air film vertically expands at the edge, reducing the pressure within a few tens of microseconds and making a rim much thicker than the interior. This thick-rimmed structure subsequently contracts into an air bubble, driven by the complex interaction between surface tension, inertia and viscous effects. Our investigation provides explicit information for the initial impact pressure as well as the detailed profile transformation during the subsequent evolution. This knowledge may benefit impact-related applications such as surface coating and splash control.

Acknowledgement

References

VAN DAM, D. B. & CLERC, C. L. 2004 Experimental study of the impact of an ink-jet printed droplet on a solid substrate. *Phys. Fluids* **16** (9), 3403–3414.

DRISCOLL, M. M. & NAGEL, S. R. 2011 Ultrafast interference imaging of air in splashing dynamics. *Phys. Rev. Lett.* **107**, 154502.

HICKS, P. D., ERMANYUK, E. V., GAVRILOV, N. V. & PURVIS, R. 2012 Air trapping at impact of a rigid sphere onto a liquid. *J. Fluid Mech.* **695**, 310–320.

HICKS, P. D. & PURVIS, R. 2010 Air cushioning and bubble entrapment in three-dimensional droplet impacts. *J. Fluid Mech.* **649**, 135–163.

KOLINSKI, J. M., RUBINSTEIN, S. M., MANDRE, S., BRENNER, M. P., WEITZ, D. A. & MAHADEVAN, L. 2012 Skating on a film of air: drops impacting on a surface. *Phys. Rev. Lett.* **108**, 074503.

MANDRE, S., MANI, M. & BRENNER, M. P. 2009 Precursors to splashing of liquid droplets on a solid surface. *Phys. Rev. Lett.* **102**, 134502.

MANI, M., MANDRE, S. & BRENNER, M. P. 2010 Events before droplet splashing on a solid surface. *J. Fluid Mech.* **647**, 163–185.

DE RUITER, J., OH, J. M., VAN DEN ENDE, D. & MUGELE, F. 2012 Dynamics of collapse of air films in drop impact. *Phys. Rev. Lett.* **108**, 074505.

SMITH, F. T., LI, L. & WU, G. X. 2003 Air cushioning with a lubrication/inviscid balance. *J. Fluid Mech.* **482**, 291–318.

THORODDSEN, S. T., ETOH, T. G. & TAKEHARA, K. 2003 Air entrapment under an impacting drop. *J. Fluid Mech.* **478**, 125–134.

THORODDSEN, S. T., ETOH, T. G., TAKEHARA, K., OOTSUKA, N. & HATSUKIH, Y. 2005 The air bubble entrapped under a drop impacting on a solid surface. *J. Fluid Mech.* **545**, 203–212.

XU, L. 2007 Liquid drop splashing on smooth, rough, and textured surfaces. *Phys. Rev.* E **75**, 056316.

XU, L., ZHANG, W. W. & NAGEL, S. R. 2005 Drop splashing on a dry smooth surface. *Phys. Rev. Lett.* **94**, 184505.

YARIN, A. L. 2006 Drop impact dynamics: splashing, spreading, receding, bouncing. *Annu. Rev. Fluid Mech.* **38** (1), 159–192.